Journal of Membrane Science 467 (2014) 85–92

Contents lists available at ScienceDirect

Journal of Membrane Science

journal homepage: www.elsevier.com/locate/memsci

Hydrogen permeability and chemical stability of Ni–$BaZr_{0.1}Ce_{0.7}Y_{0.1}Yb_{0.1}O_{3-\delta}$ membrane in concentrated H_2O and CO_2

Shumin Fang [a], Kyle S. Brinkman [b], Fanglin Chen [a,*]

[a] Department of Mechanical Engineering, University of South Carolina, Columbia, SC 29208, USA
[b] Department of Materials Science and Engineering, Clemson University, Clemson, SC 29634, USA

ARTICLE INFO

Article history:
Received 7 February 2014
Received in revised form
2 May 2014
Accepted 5 May 2014
Available online 14 May 2014

Keywords:
Hydrogen permeation
High temperature proton conductor
Chemical stability
Barium cerate
Reverse water gas shift reaction

ABSTRACT

Ni–$BaZr_{0.1}Ce_{0.7}Y_{0.1}Yb_{0.1}O_{3-\delta}$ (Ni–BZCYYb) membrane shows improved and stable performance in dry H_2 and CO_2 (Fang et al., ACS Appl. Mater. Interfaces 6 (2014) 725–730). However, the stream from steam methane reforming contains high contents of H_2O, CO_2, and CO, which poses crueler challenges to the chemical stability of Ni–BZCYYb membrane than dry H_2 and CO_2. In this work, we tested the Ni–BZCYYb membrane in wet H_2 and CO_2 which generated high content of H_2O and CO due to reverse water gas shift (RWGS) reaction at high temperature. High content of H_2O improves the proton conductivity of BZCYYb and hydrogen transport through the membrane. On the other hand, H_2 content reduction and decomposition of BZCYYb promoted by high content of H_2O lead to performance degradation. The steady-state hydrogen flux may increase or decrease depending on the balance among these effects. Besides, CO-induced Ni corrosion was found in both surface and bulk due to metal dusting. In general, Ni–BZCYYb membrane still displayed much better performance stability in wet H_2 and CO_2 than Ni–$BaCe_{0.8}Y_{0.2}O_{3-\delta}$ and Ni–$BaZr_{0.1}Ce_{0.7}Y_{0.2}O_{3-\delta}$ composites, making it a candidate material system for further studies aimed at membrane processing of hydrocarbons.

1. Introduction

As an important feedstock for the production of ammonia and hydrocarbons, hydrogen is consumed in large quantity to meet the ever-growing demand for food and liquid fuels. Due to the high oil price and decreasing crude oil reserves, the production of liquid fuels from heavy petroleum sources (especially from tar sands and oil shale) increases rapidly, consuming even more hydrogen than before [1]. Currently, most hydrogen is produced through steam methane reforming (SMR), followed by two-step water gas shift reaction and pressure swing absorption process for H_2/CO_2 separation [2]. These complex processes are both capital and energy intensive. Hydrogen separation membranes like Ni–$BaZr_{0.1}Ce_{0.7}Y_{0.2}O_{3-\delta}$ (Ni–BZCY) and Ni–$BaZr_{0.1}Ce_{0.7}Y_{0.1}Yb_{0.1}O_{3-\delta}$ (Ni–BZCYYb) have demonstrated high hydrogen permeability [3–6], which can be used for direct extraction of hydrogen from the exhaust stream of SMR. The combination of distinct unit operations into a single membrane reactor results in process intensification and is expected to significantly reduce the cost of hydrogen production [3]. The exhaust stream from SMR contains about 76% H_2 (mol%), 13% CH_4, 12% CO and 10% CO_2 on a dry basis [7]. A high steam/methane ratio of 2.5 is normally used to obtain high methane conversion, leading to a significant amount of moisture in the stream. The high content of H_2O and CO_2 in the exhaust stream from SMR poses a significant challenge to the chemical stability of the hydrogen permeation membrane and must be addressed before implementation of this promising technology.

The poor chemical stability of $BaCeO_3$ in H_2O and CO_2 has been one of the major obstacles for its applications in intermediate temperature solid oxide fuel cells and hydrogen separation membranes [8–10]. Considerable efforts have been made to improve the chemical stability of $BaCeO_3$. In, Sn, Ti, Zr, Nb, and Ta-doped barium cerates show different degrees of improved tolerance towards H_2O and CO_2, although this is coupled with a decrease in proton conductivity [11–17]. Among these materials, Zr-doped $BaCeO_3$ shows the best compromise between proton conductivity and chemical stability [3,18–20]. The flux of Ni–BZCY membrane still suffers serious degradation in wet H_2 and CO_2 due to the formation of insulating $BaCO_3$ on the membrane surface [3]. Recently, we have discovered that the flux of Ni–BZCYYb membrane greatly increased after CO_2 was introduced into dry H_2-containing feed gas [6]. The reverse water gas shift reaction (RWGS) between H_2 and CO_2 generated H_2O, increased

* Corresponding author. Tel.: +1 803 7774875; fax: +1 803 7770106.
E-mail address: chenfa@cec.sc.edu (F. Chen).

http://dx.doi.org/10.1016/j.memsci.2014.05.008
0376-7388/

the proton conductivity of $BaZr_{0.1}Ce_{0.7}Y_{0.1}Yb_{0.1}O_{3-\delta}$ (BZCYYb), and thus promoted the hydrogen permeation. However, the performance increase became less prominent when the CO_2 content further increased. It is unclear whether the performance improvement in CO_2 is still observable in wet H_2. Furthermore, the performance of Ni–BZCYYb was very stable during a 540-h-long test in dry 20% H_2 and 20% CO_2 at 900 °C with low moisture content (<3 vol% H_2O). However, the chemical stability of $BaCeO_3$ in concentrated H_2O and CO_2 may be worse than that in CO_2 with a low moisture content. The extent of reaction between CO_2 and $Sr_{0.95}Co_{0.8}Fe_{0.2}O_{3-\delta}$ or $La_{1-x}Sr_xFe_{0.8}Cr_{0.2}O_{3-\delta}$ has been reported to be significantly higher in wet CO_2 than in dry CO_2 [21,22]. It is unclear whether BZCYYb displays similar behavior in CO_2 with concentrated H_2O.

In order to clarify these important issues, permeation flux of Ni–BZCYYb membrane was measured in wet H_2 and CO_2 at 900 °C. The performance stability was studied in different H_2 and CO_2 contents to obtain more insights on the effect of reverse water gas shift reaction. The effects of H_2O, CO, and CO_2 on the phase composition and microstructure of tested membrane was investigated through XRD, SEM-EDX, and Raman analysis.

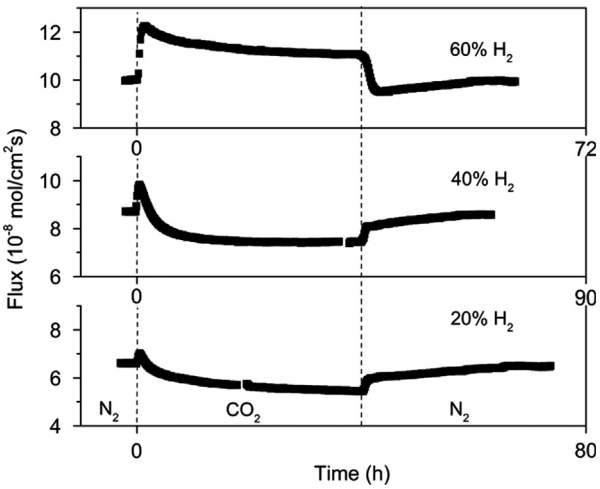

Fig. 1. Time dependence of hydrogen flux of a 0.56-mm-thick membrane in X% H_2 balanced with 3% H_2O, 30% CO_2, and $(67-X)$% He. $X=20$, 40, and 60, respectively.

2. Experimental

BZCYYb powder was synthesized by a sol–gel combustion method and calcined at 1100 °C for 5 h [6]. Ni powder (Alfa Aesar, ~325 mesh, 99.8% metal basis) and BZCYYb powder were then carefully mixed in volume ratio of 40:60 using agate mortar and pestle. The mixed powder was pressed in a 20-mm stainless steel die and sintered at 1440 °C for 10 h in 5% H_2/N_2 to obtain dense Ni–BZCYYb membrane.

The membrane was tested in a set-up for hydrogen permeability measurements [6]. Both surfaces of the sintered Ni–BZCYYb membrane were polished with silicon carbide sandpapers (120, 320, 600 grits) before the hydrogen permeation measurement. The Ni–BZCYYb membrane was sealed using two glass rings to two vertical alumina tubes. To prevent exposure of the membrane to air, the edge of the membrane was first covered with glass powder (Schott 8252) well-dispersed in terpineol, dried, and then covered by a ceramic-glass sealant (Aremco, C552). The sealing was achieved by curing at 90, 230, 1000 °C for 3, 3, and 1 h, respectively. The feed gas is a mixture of H_2 balanced with He (Airgas, 99.9993%) and N_2 (Airgas, 99.9993%)/CO_2 (Airgas, 99%) with a total flow rate of 100 mL/min using mass flow controllers (Apex Vacuum Schoonover Inc). The feed gas was mixed in a 500 mL 4-neck glass flask and then passed a water bubbler containing distilled water to obtain wet feed gas. The sweep gas was 20 mL/min N_2. The composition of the exhaust from both feed and sweep side was analyzed by a gas chromatograph (GC, Agilent 7890A) equipped with two thermal conductivity detectors using ultra carrier grade N_2 and He as carrier gases, respectively. The GC was regularly calibrated by standard gas (Airgas). The flow rate of the exhaust from the sweep side was measured by a digital flow meter (Agilent ADM2000). The leakage through incomplete sealing was checked by measuring helium concentration in the sweep gas. No helium was detected, suggesting that an effective sealing was obtained.

X-ray diffraction (XRD, Rigaku D/Max 2100, with Cu Kα radiation) analysis was used to identify the phases present in the powder and pellets. Field emission scanning electron microscopy (FESEM, Zeiss ultra plus) equipped with an energy dispersive spectroscopy (EDS, Oxford) were used to study the microstructure and chemical composition of the Ni–BZCYYb membranes. Raman spectrum of tested membrane was recorded using a LabRam/HR confocal Raman system (LabRam Invers, Horiba Jobin-Yvon) with a He–Ne laser operated at 632.8 nm.

3. Results

Fig. 1 shows the hydrogen flux change in wet feed gas with different hydrogen content (20, 40, and 60 vol%, respectively) after the introduction and removal of 30% CO_2. Two processes are observed after the introduction of CO_2. In the first process, the hydrogen permeation fluxes quickly increase. Interestingly, the hydrogen permeation flux increase is found to increase with the hydrogen content. In the second process, the fluxes slowly decrease. The steady-state hydrogen permeation flux can be higher (in the case of 60% H_2) or lower (in the cases of 20% H_2 and 40% H_2) than the initial hydrogen permeation flux depending on the balance between the flux increase and decrease in the first and second processes, respectively. After introduction of 30% CO_2, the CO contents in the feed gas containing 20, 40, and 60% H_2 are 3.8%, 8.5%, and 7.2%, respectively. The increase of CO content stems from the RWGS reaction:

$$H_2(g)+CO_2(g)=H_2O(g)+CO(g) \quad (1)$$

After the removal of CO_2, the hydrogen flux first changes quickly (decrease in 60% H_2 while increase in both 40% and 20% H_2) and then gradually increases to the original value prior to the introduction of CO_2. The increase of hydrogen permeation flux after removal of CO_2 is called the recovery process, which is also observed in studies of oxygen permeation membranes tested in CO_2 [23,24]. In wet 40% H_2 and 30% CO_2, the hydrogen permeation flux of Ni–BZCYYb membrane decreased from 8.8 to 7.7×10^{-8} mol/(cm^{2}s), which is 11.4% reduction in performance. In comparison, the hydrogen permeation fluxes of Ni–BZCY membrane decreased 42.3%, and the hydrogen permeation fluxes of Ni–$BaCe_{0.8}Y_{0.2}O_{3-\delta}$ (Ni–BCY) membrane reduced to zero in the same condition [3]. The performance stability of Ni–BZCYYb membrane is much better than that of Ni–BZCY and Ni–BCY membrane.

Fig. 2 presents the hydrogen permeation flux change in wet feed gas containing 40% H_2 after the introduction of 10, 20, 30, and 40 vol% CO_2, respectively. Prior to the introduction of CO_2, the hydrogen permeation flux was 8.8×10^{-8} mol/(cm^{2}s). After 10% CO_2 was introduced to the feed gas stream, the hydrogen permeation flux increased to 10.0×10^{-8} mol/(cm^{2}s) but then gradually decreased to 9.5×10^{-8} mol/(cm^{2}s). When the CO_2 concentration was subsequently increased to 20%, 30%, and 40%, the hydrogen

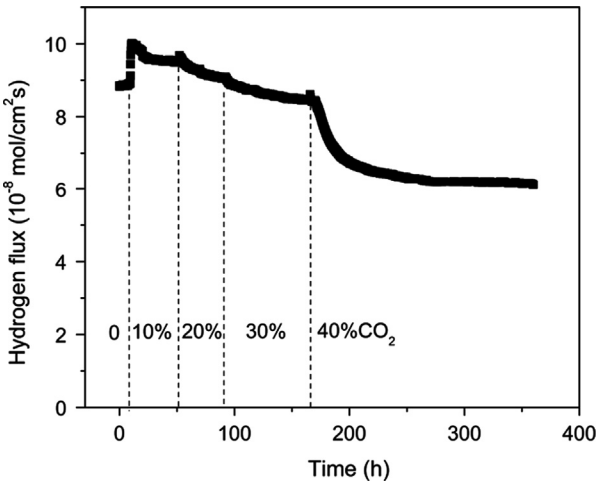

Fig. 2. Time dependence of hydrogen permeation flux of a 0.56-mm-thick Ni–BZCYYb membrane in 40% H_2, 3% H_2O, *X*% CO_2, and (57 − *X*)% He. *X* changes from 0, 10, 20, 30, to 40 with time as indicated in the figure.

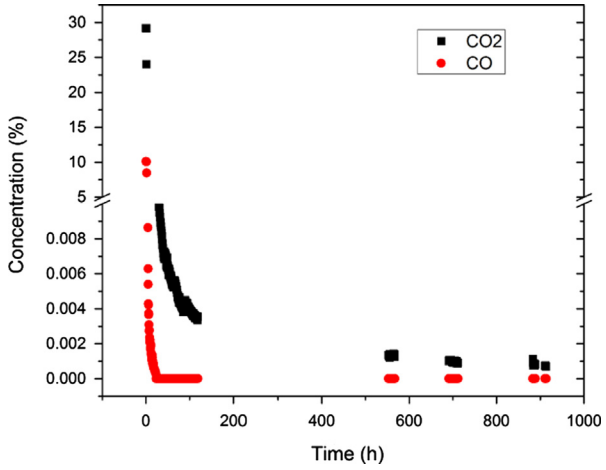

Fig. 3. Time dependence of CO_2 and CO concentration when CO_2 was replaced by N_2. Feed gas contained 20% H_2, 3% H_2O, 17% He, 60% CO_2/N_2. The CO concentration was below detection limit after 9 h.

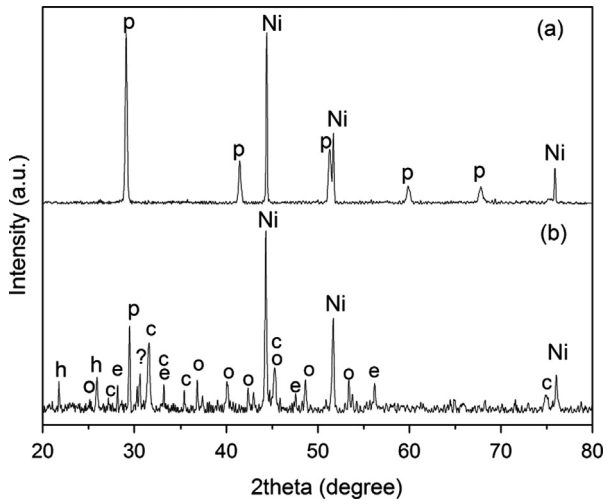

Fig. 4. XRD patterns obtained from the fresh (a) and tested (b) Ni–BZCYYb membrane. p: BZCYYb, h: hexagonal $BaCO_3$ [25], o- orthorhombic $BaCO_3$ [23,25], c: carbon (JCPDS 46-0943), e: doped-CeO_2 [25], ?: unknown phase.

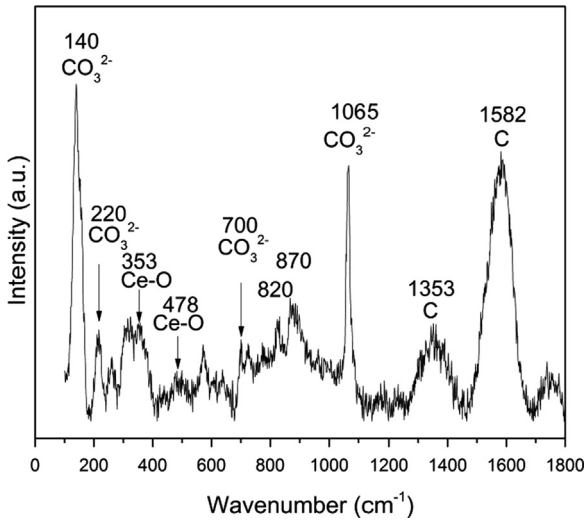

Fig. 5. Raman spectrum obtained from feed side surface of Ni–BZCYYb membrane after exposure to wet CO_2 and recovery without CO_2.

permeation flux decreased to 9.1, 8.5, 6.2×10^{-8} mol/(cm^{2}s), respectively.

After the permeation test in the presence of CO_2, the Ni–BZCYYb membrane was recovered in wet 40% H_2/N_2/He for ~912 h at 900 °C followed by furnace cooling in the same atmosphere. During the recovery process, the concentrations of CO and CO_2 were monitored by GC and shown in Fig. 3. The initial contents of CO_2 and CO were 29.2% and 10.1%, respectively. Both contents quickly decreased after CO_2 was replaced by N_2. No CO could be detected after ~20 h. However, a small amount of CO_2 (~8 ppm) was still detectable even after 912 h.

The XRD patterns of Ni–BZCYYb membrane before and after the permeation test in CO_2 are shown in Fig. 4. The pattern of fresh Ni–BZCYYb membrane only shows the peaks corresponding to perovskite and Ni phases, suggesting that Ni and BZCYYb phases are obtained after sintering in reducing atmosphere. However, the XRD pattern obtained from feed side of the tested and recovered sample shows that the surface consisted of Ni, BZCYYb, $BaCO_3$, doped-CeO_2, carbon, and some minor unknown phases. The peaks for both hexagonal and orthorhombic $BaCO_3$ are found [23,25]. At 900 °C, $BaCO_3$ exists in the form of hexagonal phase. During the fast cooling process, a hexagonal–orthorhombic phase transition takes place at around 810–850 °C [25]. Therefore, both phases can be found.

Fig. 5 shows the Raman spectrum obtained from the surface of the feed side in Fig. 4b. The bands at 140, 220, 700, and 1065 cm^{-1} belong to CO_3^{2-} [25,26], confirming the existence of $BaCO_3$ found by XRD and the decomposition of BZCYYb in wet CO_2. The peak near 470 cm^{-1} can be assigned to F2g Raman-active mode of CeO_2 [25,27]. The peak near 353 cm^{-1} can be assigned to Ce–O bond in $BaCeO_3$ [25]. The existence of doped-$BaCeO_3$ suggests $BaCO_3$ and doped-CeO_2 react forming doped-$BaCeO_3$ again after CO_2 has been removed from the feed gas. Bands for carbon can be found at 1353 and 1582 cm^{-1} [28]. Carbon may come from the disproportionation reaction of CO and/or the reaction between H_2 and CO [28–30]. The bands at 820 and 870 cm^{-1} have been assigned to hydrogen carbonate and polydentate carbonate, respectively [31]. The observation of $BaCO_3$, doped-$BaCeO_3$, doped-CeO_2, and carbon from the Raman spectrum is in good agreement with the XRD results in Fig. 4b.

The microstructure of the tested Ni–BZCYYb membrane was analyzed by SEM-EDX. Fig. 6a shows the cross-sectional view of the entire Ni–BZCYYb membrane. The tested membrane is thicker than fresh membrane (0.56 mm), especially in the center

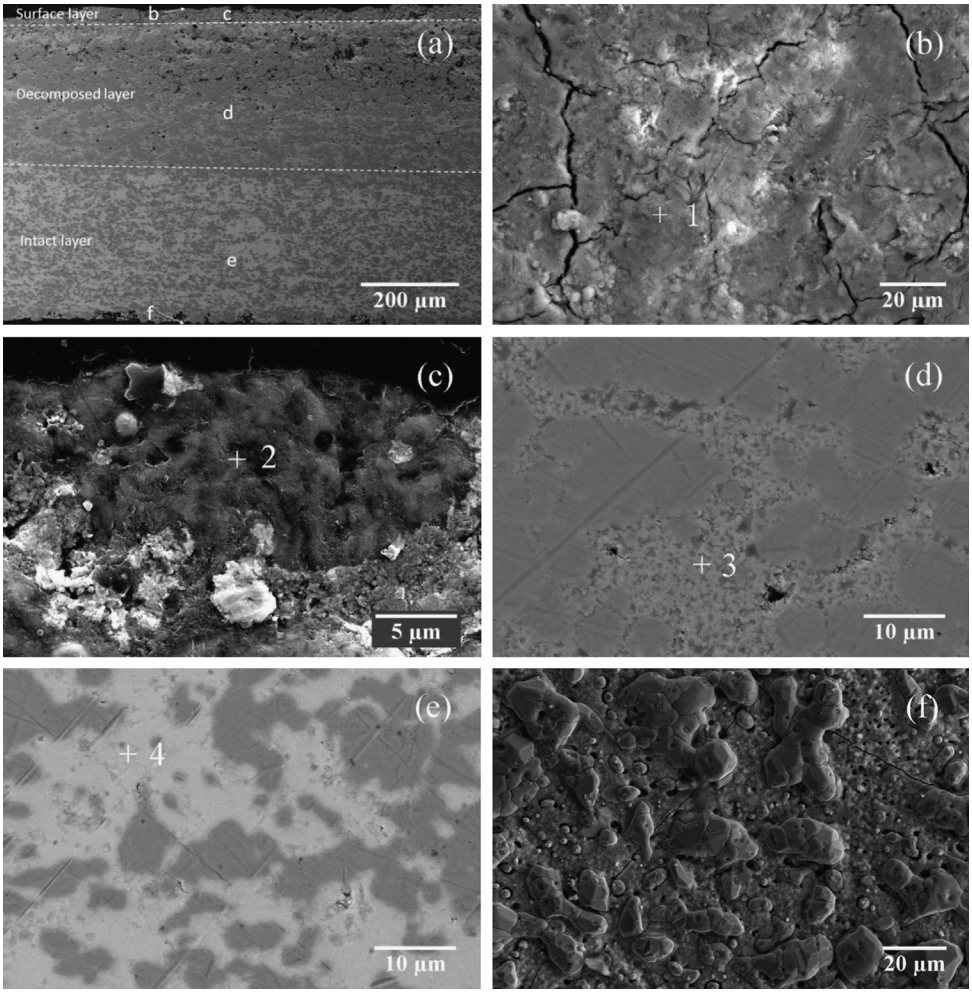

Fig. 6. SEM images of Ni–BZCYYb membrane tested in CO_2, recovered and cooled without CO_2. (a) Full cross-sectional view; (b) feed side surface from top view; (c) part of surface layer taken in position c; (d) part of decomposed layer taken in position d; (e) part of intact layer taken in position e; and (f) sweep side surface from bottom view. Surfaces were not polished prior to SEM study. Cross-section was polished prior to SEM study. All images are taken in second electron image mode (SEI), except that Fig. 6e is taken in back scattered electron image mode (BSE).

(0.66 mm, right side of Fig. 6a), suggesting that it expands during the test. Based on the characteristics of microstructure, the cross-section of membrane is divided into three distinct areas: surface layer (with a thickness around 20–30 μm), decomposed layer (with a thickness around 280–310 μm), and intact layer (with a thickness around 320 μm), which are magnified in Fig. 6c, d, and e, respectively. Fig. 6b shows the microstructure of the surface layer from top view. In contrast to clear BZCYYb and Ni grains observable in fresh membrane [6], no clear ceramic or Ni grains can be found. Instead, the surface is entirely covered by a layer of dust-like phase with many cracks. The magnified cross-sectional view of the surface layer in Fig. 6c shows that the thickness of dust-like layer is ~20 μm. Fig. 7a and b shows the EDX spectra obtained from spots 1 and 2 from Fig. 6b and c, respectively. Both spectra show that there are only Ba, C, O, Au (from gold sputtering before SEM analysis). No nickel particles are observed by SEM on the surface in Fig. 6b, although the peaks of Ni are found in the XRD pattern. It is known that Ni can be corroded in superabundant carbon environment, leading to metal dusting on the surface and growth of Ni metal in the bulk which will be discussed later [29]. Although BZCYYb and doped ceria are found by XRD, they are not observed by SEM-EDX. This is probably due to the difference in their detection depth. SEM-EDX can only reach the sample surface, while XRD can reach a few micrometers in depth depending on the density of the sample. Some BZCYYb and doped ceria particles are probably covered by $BaCO_3$ on the top surface.

The microstructure of the intact layer (Fig. 6e) is similar to that of fresh membrane. The dark and light phases are Ni and BZCYYb phases, respectively. They are randomly distributed and form a very dense microstructure. The content of Ni phase is apparently smaller than that of BZCYYb phase, which is consistent with the volume ratio of Ni and BZCYYb (40:60). In contrast, both the content and size of Ni particles in the decomposed layer increases with reducing depth from the surface layer (Fig. 6a). This is in agreement with the description of carbon-induced Ni corrosion: Ni particles expand after carbon diffusion and precipitation in Ni bulk [29]. The expansion causes the increase of membrane thickness, especially in the center of the membrane (right side in Fig. 6a) where the feed gas directly strikes. The decomposed layer is porous in the top part (Fig. 6a) but rather dense in the bottom part (Fig. 6d). All the gases can freely penetrate through the porous part but not the dense part. Therefore, the decomposed layer was selectively permeable to H_2 in the dense part but not in the porous part, leading to a reduction in the effective thickness of permeation layer, which is beneficial for the hydrogen permeation. Therefore, although the thickness of the tested membrane (0.63 mm in the center) is thicker than that of the fresh membrane (0.56 mm), the hydrogen flux returns to initial value after the recovery process. Nickel dusting also leads to

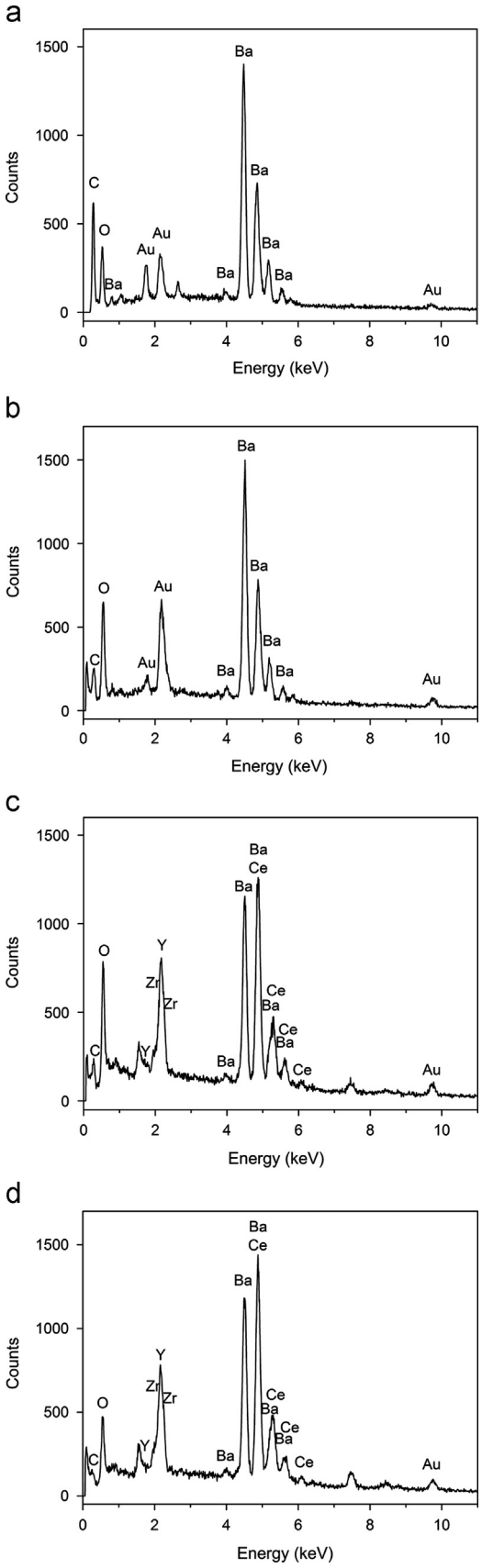

Fig. 7. EDX spectra obtained from spots 1 (a), 2 (b), 3 (c), and 4 (d) in Fig. 6.

decrease in relative volume ratio of BZCYYb phase in decomposed layer. Unlike the smooth surface in the intact layer, the ceramic phase in the decomposed layer shows a rough surface with many small particles ($<1\,\mu m$, Fig. 6d). Fig. 7c and d shows the EDX spectra obtained from spots 3 and 4 in Fig. 6d and e, respectively. Similar chemical composition (Ba, Ce, Y, Zr) of ceramic phase was found in the decomposed layer and intact layer, suggesting the BZCYYb phase is restored (at least partly) in the decomposed layer after the long recovery process. On the sweep side surface (Fig. 6f), Ni particles with size $\sim$10–30 μm are embedded in fine ceramic particles.

In general, the microstructure and phase composition study shows the decomposition of the BZCYYb ceramic phase and corrosion of Ni caused by formation of carbon during the exposure to concentrated H_2O, CO, and CO_2. The former generates doped ceria and $BaCO_3$, leading to performance degradation, while the latter causes the growth of Ni particles and reconstruction of membrane microstructure in the decomposed layer.

4. Discussions

Unlike the stable performance and high chemical stability observed in dry H_2 and CO_2 [6], the fluxes of Ni–BZCYYb degrade after initial increase and phase decomposition is observed in wet H_2 and CO_2. This is coupled with much higher moisture contents in the wet H_2 and CO_2 than that in dry H_2 and CO_2. The total water content in Fig. 1 (6.8–11.5%, sum of the moisture from the bubbler and the RWGS reaction) is much higher than that in dry H_2 and CO_2 (0.5–2.2%) in our previous report [6]. Apparently, BZCYYb reacts with CO_2 in concentrated H_2O and CO_2 but not in CO_2 with low H_2O content at 900 °C, suggesting that the reaction between BZCYYb and CO_2 is enhanced by high H_2O content. To the best of our knowledge, there are no reports on this co-operative degradation behavior in $BaCeO_3$-based perovskite oxides. This singular behavior may be caused by several mechanisms. Firstly, high content of H_2O may react with $BaCeO_3$ generating CeO_2 and Ba $(OH)_2$ which subsequently reacts with CO_2 forming $BaCO_3$. However, thermodynamic calculation indicated that $BaCeO_3$ was stable in $<18.8\%$ H_2O at 900 °C and annealing experiments showed that $La_{0.05}BaCe_{0.95}O_{3-\delta}$ was stable in 56.8% H_2O at 900 °C [32]. Therefore, it is unlikely that BZCYYb first reacts with H_2O. Secondly, H_2O and CO_2 form van der Waals complex which may subsequently react with BZCYYb to form barium bicarbonate. Yi et al. reported that the oxygen permeation flux of $Sr_{0.95}Co_{0.8}Fe_{0.2}O_{3-\delta}$ was stable in the presence of CO_2 alone, but not stable in the presence of both CO_2 and H_2O [21]. Similar behavior was observed for $La_{1-x}Sr_xFe_{0.8}Cr_{0.2}O_{3-\delta}$ by Kaus et al. [22]. They attributed this behavior to the formation of bicarbonates through van der Walls complex. Therefore, it is reasonable to assume that a similar mechanism is working in our case: high level of H_2O promotes the reaction between BZCYYb and CO_2, forming $BaCO_3$ and doped ceria particles mixed with Ni, consistent with the XRD and SEM-EDX observations.

The H_2O and CO contents in wet H_2 and CO_2 are much higher than those in dry H_2 and CO_2, suggesting RWGS reaction proceeds and generates more products (water and CO, see Eq. (1)) when there is already a high water content. If the system is in chemical equilibrium state, the addition of more product (H_2O) should drive the reaction back, which is contrary to our results. Besides, the chemical equilibrium constant of RWGS reaction at 900 °C is $\sim$1.3 (calculated through HSC chemistry 6.0 software), which means that the contents of CO and H_2O should be higher than those of H_2 and CO_2 in chemical equilibrium state. However, the amounts of CO and H_2O are much smaller than those of H_2 and CO_2 in our study. These results suggest that the system is not in chemical equilibrium state, but controlled by kinetics factors, which can be accelerated by catalysts. Fine doped-CeO_2 particles provide an excellent catalytic activity for the RWGS reaction, and the activity

can be greatly promoted by the addition of metals like Pt, Cu, and Ni [33,34]. The formation of porous surface and decomposed layers also extends the contact time of the gases with catalyst. In this way, the decomposition reaction of BZCYYb and RWGS reaction become mutually reinforcing. More water leads to formation of more Ni/doped-CeO_2 catalyst and extended contact time, which promotes the RWGS reaction and generates more water.

This mechanism can easily explain the difference observed in dry and wet feed gases. In dry H_2 and CO_2, the initial H_2O content is very low that the reaction between BZCYYb and CO_2 is inhibited, and no doped-ceria catalyst is generated for the RWGS reaction. Consequently, the RWGS reaction is slow, generating only a small amount of H_2O and CO. The CO content was only 1.6% and 2.2% in dry 20% H_2 after introduction of 40% and 60% CO_2, respectively [6]. In wet H_2 and CO_2, the initial H_2O content is much higher (considering both water introduced from the water bubbler and water produced from the initial RWGS reaction). Therefore, the reaction between BZCYYb and CO_2 is promoted, generating much more doped-CeO_2, which provides catalytic activity for RWGS reaction after coupling with Ni. The RWGS is therefore accelerated and produces much more H_2O, which in turn promotes the reaction between BZCYYb and CO_2. Therefore, the accelerated RWGS reaction leads to both direct and indirect effects on the performance of Ni–BZCYYb membrane in CO_2: improve the hydrogen permeation flux by increasing H_2O content, decrease the hydrogen permeation flux by reducing H_2 content, and promoting the decomposition of BZCYYb. The high CO content also leads to Ni corrosion and microstructure reconstruction of the membrane. A schematic of these effects is shown in Fig. 8 to promote understanding. These effects are discussed in detail as follows.

First, the accelerated RWGS reaction greatly increases the H_2O content in the feed gas, improving the proton conductivity of BZCYYb phase and hydrogen flux of Ni–BZCYYb membrane. In all of the experiments conducted in this study, a hydrogen permeation flux increase was found in wet feed gas when CO_2 was introduced, which resembled that in dry feed gas [6]. It is noticed that the relative hydrogen permeation flux increase after the introduction of CO_2 in initially dry H_2 is much larger than that in wet H_2 in this study. This is expected because the proton conductivity improvement is less significant in wet atmosphere where BZCYYb is close to the solubility limit of protonic defects. As more and more H_2O is dissolved in the bulk phase, BZCYYb is finally saturated with H_2O and further increase in H_2O content cannot improve the proton conductivity and therefore hydrogen permeation flux [6].

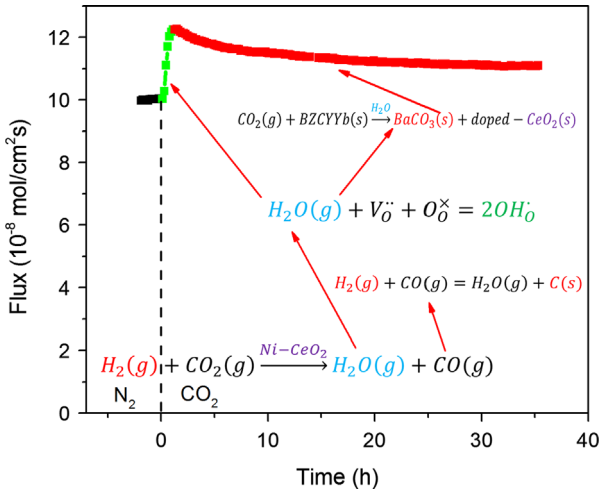

Fig. 8. Schematic of the processes after 30% CO_2 was introduced into wet 60% H_2. Factors that lead to increase or decrease of flux are marked in green and red, respectively. (For interpretation of the references to color in this figure legend, the reader is referred to the web version of this article.)

It can be seen in Fig. 1 that the hydrogen permeation flux enhancement increases with increasing hydrogen content. The hydrogen permeation flux through BZCYYb phase in Ni–BZCYYb membrane is determined by:

$$J = \frac{RT\sigma\Delta p^{1/2}}{2F^2L} \quad (2)$$

where J, R, T, σ, $\Delta p^{1/2}$, F, and L are the flux, ideal gas constant, temperature, proton conductivity, the difference of the square roots in hydrogen partial pressure between feed and sweep gases, Faraday constant, and membrane thickness, respectively [6]. When all the other factors (T, L) are the same, the hydrogen permeation flux increase in the BZCYYb phase was due to proton conductivity (σ) increase and was proportional to difference of the square roots in hydrogen partial pressure between feed and sweep gases ($\Delta p^{1/2}$). The high moisture contents (10.2% and 11.5% for the cases of 60% and 40% H_2, respectively) resulted in the saturation of the protonic defects in the BZCYYb material and comparable levels of proton conductivity. In 20% H_2, H_2O content was the lowest (only 6.8%), and the proton conductivity was also the lowest. Besides, $\Delta p^{1/2}$ follows the order of hydrogen content. Therefore, the hydrogen permeation flux enhancement (proportional to $\Delta\sigma\Delta p^{1/2}$) also follows the order of hydrogen content.

Second, the accelerated RWGS reaction significantly reduces the H_2 content and thus the driving force for hydrogen permeation. In Fig. 1, the hydrogen permeation flux decrease caused by reduced hydrogen content (16.2% and 31.5% H_2 compared with the initial 20% and 40% H_2, respectively) has been estimated to be 10.3% and 11.5% (according to Fig. 3 in our previous report [6]) compared with the total hydrogen permeation flux decrease of 14.4% and 19.2%, respectively, observed in this work. The decrease of hydrogen permeation flux was not observed in dry H_2 and CO_2 although RWGS reaction also took place [6]. This is because the extent of the RWGS reaction in dry H_2 and CO_2 is much lower than that in wet H_2 and CO_2. The minor effect was probably covered by the significant hydrogen flux enhancement due to sharp increase in moisture content.

Third, the reaction between CO_2 and BZCYYb is promoted under wet CO_2 conditions and generated more $BaCO_3$ in wet H_2 and CO_2 than that in dry H_2 and CO_2. The post-experimental phase composition and microstructure analysis clearly shows the formation of $BaCO_3$. This is similar to the result of Ni–BZCY membrane in wet H_2 and CO_2 [3]. Because BZCYYb phase reacted with CO_2 forming $BaCO_3$ on the surface, the ceramic layer close to the surface was depleted with Ba^{2+}, generating a chemical potential for Ba^{2+} in the bulk to diffuse to the surface, forming additional $BaCO_3$. Yi et al. investigated the oxygen permeation behavior of $BaCo_{0.4}Fe_{0.4}Nb_{0.2}O_{3-\delta}$ (BCFN) after exposure to CO_2 [35]. A dense $BaCO_3$ layer was formed on top of BCFN membrane, beneath which a porous layer was found and the decomposition process was controlled by the ionic diffusion of Ba^{2+} from the bulk to the surface. In a similar way, our study also shows that change of the membrane microstructure occurred not only on the surface but also into a profound depth of ~300 μm. Because there are some cracks in the surface layer, H_2, CO, and CO_2 can penetrate into a deep layer. H_2 permeated to the other side resulting in a hydrogen flux. CO and CO_2 continued to react with Ni and BZCYYb, respectively, and gradually reached into the interior of the membrane.

It is surprising that $BaCO_3$ still exists on the surface after the 912-h-long recovery process, although the hydrogen permeation flux was completely restored. When CO_2 was switched back to N_2 at 900 °C during the recovery process, $BaCO_3$ mixed with doped ceria will react forming barium cerate again, following the

synthesis process of $BaCeO_3$. Lee et al. calcined a precursor containing $BaCO_3$ and CeO_2 between 800 and 1000 °C for 4 h [36]. The XRD patterns of calcined powders showed that the main phase was already $BaCeO_3$ and only a little $BaCO_3$ and CeO_2 were left at 850 °C. At 900 °C, the $BaCeO_3$ phase was already pure. However, $BaCO_3$ alone on the surface will sustain due to a higher decomposition temperature requirement. Thermogravimetric studies revealed that $BaCO_3$ and doped-ceria began to react and form doped $BaCeO_3$ in N_2 at ~850–900 °C [37,38], while $BaCO_3$ started losing weight in N_2 above 930–975 °C [37,39]. This explains why $BaCO_3$ remained on the surface after the 912 h recovery process at 900 °C. Underneath the surface layer, the mixture of $BaCO_3$ and doped CeO_2 slowly reacted, forming doped-$BaCeO_3$ and generating a very low concentration of CO_2 which was detected by GC (Fig. 3). However, the recovered $BaCeO_3$ grains were small because they were not sintered as that in the fresh membrane and the intact layer. At this point, it is unclear whether all the $BaCO_3$ and doped-ceria react forming $BaCeO_3$ in the decomposed layer, and further study is required to clarify this.

Fourth, the high CO content leads to Ni corrosion in a process called metal dusting [29]. This leads to permanent change in the membrane microstructure and cannot be recovered by the removal of CO_2. The Ni particles grow much bigger and the membrane becomes thicker with increased porosity. However, this does not seem to cause the performance degradation, probably because it forms a porous layer rather a dense blocking layer. When CO_2 is removed, $BaCO_3$ reacts with doped ceria forming $BaCeO_3$ and the performance recovers completely, but the microstructure change caused by Ni corrosion is persistent. Although the effect of Ni corrosion on performance is not obvious, it may cause the failure of the membrane given enough time. CO has not been thought to be harmful to Ni–$BaCeO_3$-based cermet membrane. Our study suggests that high content of CO can be detrimental to the membrane integrity and mechanical strength. Because CO is also found in the gas stream in SOFC anodes using hydrocarbon fuels, one may have concern for the dusting of Ni-based anode. The dusting of Ni in anodes should be less severe than that in hydrogen permeation membranes. This is due to the difference in their environments. Hydrogen permeation membranes are used in a very reducing atmosphere and there is no source of oxygen to oxidize the carbon. However, in the anodes of working SOFCs, there is a constant supply of oxygen through the electrolyte. The oxygen flow can greatly improve the carbon resistance of Ni-based anodes. For example, the coking resistance of SOFCs based on Ni–BZCYYb anode with $Sm_{0.1}Ce_{0.9}O_{2-\delta}$ (SDC) electrolyte was much better than that with YSZ electrolyte in dry C_3H_8 at 750 °C due to the higher oxygen ionic conductivity of SDC than that of YSZ [19], because SDC had a much higher oxygen ionic conductivity than YSZ at the testing temperature (750 °C).

Based on the above analysis, the complex flux behaviors observed in Fig. 1 can be well explained. When CO_2 was introduced, the hydrogen permeation flux increased due to sharp increase in moisture content as a result of the RWGS reaction, but gradually decreased due to reduction in H_2 content and decomposition of BZCYYb coupled with formation of $BaCO_3$. When CO_2 was removed, the hydrogen permeation flux decreased due to decrease in the moisture content, and increased due to increase in H_2 content and decomposition of $BaCO_3$. The slow degradation/recovery process should be due to the formation/decomposition of $BaCO_3$ for the following reasons: (i) the change in H_2, CO, and H_2O content is very fast (completed in just a few hours, Fig. 3), (ii) a small concentration of CO_2 was detected in the feed gas for 912 h indicating slow decomposition of $BaCO_3$ (Fig. 3), and (iii) the existence of $BaCO_3$ after recovery for 912 h also indicated that the decomposition of $BaCO_3$ was very slow. The fast degradation/recovery process was due to the change in H_2O and H_2 contents. The result of the fast recovery process depended on the competition between the increase in flux due to H_2 content increase and the decrease in flux due to the decrease in H_2O content. The change in hydrogen flux due to change in H_2O content increased with increasing hydrogen content in feed gas. The flux change due to changes in hydrogen content was greater at low hydrogen content than at high hydrogen content [6]. Therefore, the fast flux decrease due to the decrease in H_2O content was dominant in a feed gas with 60% H_2, while a flux increase due to H_2 content increase was dominant in feed gas with 40% and 20% H_2. Therefore, the flux first decreased in 60% H_2 but increased in 20% and 40% H_2 in the recovery process. After this fast process, the flux slowly recovered to initial value due to decomposition of $BaCO_3$ and regeneration of $BaCeO_3$.

5. Conclusions

The RWGS reaction in wet H_2 and CO_2 became more pronounced than that in dry H_2 and CO_2. This produced more H_2O and promoted proton conductivity of BZCYYb. The flux enhancement increased with initial hydrogen content but decreased with initial water content in the feed gas. In addition, the high content of H_2O promoted the reaction between CO_2 and BZCYYb forming insulating secondary phases and causing performance degradation. Besides, Ni corrosion due to high content of CO formed in feed gas is found to cause Ni growth and microstructure reconstruction of membrane. The hydrogen permeation behavior of Ni–BZCYYb membrane is the combined result of these effects. Depending on the exact feed gas concentration of H_2, CO_2, and H_2O, the final hydrogen permeation flux may rise or fall after the introduction of CO_2. Unlike the Ni–BZCY or Ni–BCY membrane which suffers significant hydrogen permeation flux decrease (42.3% and 100%, respectively) in wet 30% CO_2 at 900 °C, Ni–BZCYYb membrane demonstrates minor performance degradation (11.4%) under such conditions. These results show that a Ni–BZCYYb membrane material is very promising for applications of hydrogen separation in the presence of CO_2 and highlight the important potential that proton-conducting ceramic materials for future membrane separations processes.

Acknowledgments

We gratefully acknowledge the financial support from the DOE Office of Nuclear Energy's Nuclear Energy University Program under award # 10-681 and the SCUREF/SRNS/DOE under award # B139006.

References

[1] J. Martínez, J.L. Sánchez, J. Ancheyta, R.S. Ruiz, A review of process aspects and modeling of ebullated bed reactors for hydrocracking of heavy oils, Catal. Rev.-Sci. Eng. 52 (2010) 60–105.
[2] I. Martínez, M.C. Romano, P. Chiesa, G. Grasa, R. Murillo, Hydrogen production through sorption enhanced steam reforming of natural gas: thermodynamic plant assessment, Int. J. Hydrog. Energy 38 (2013) 15180–15199.
[3] C. Zuo, S.E. Dorris, U. Balachandran, M. Liu, Effect of Zr-doping on the chemical stability and hydrogen permeation of the Ni–$BaCe_{0.8}Y_{0.2}O_{3-\delta}$ mixed protonic-electronic conductor, Chem. Mater. 18 (2006) 4647–4650.
[4] Z. Zhu, W. Sun, L. Yan, W. Liu, W. Liu, Synthesis and hydrogen permeation of Ni–$Ba(Zr_{0.1}Ce_{0.7}Y_{0.2})O_{3-\delta}$ metal-ceramic asymmetric membranes, Int. J. Hydrog. Energy 36 (2011) 6337–6342.
[5] M. Liu, W. Sun, X. Li, S. Feng, D. Ding, D. Chen, M. Liu, H.C. Park, High-performance Ni–$BaZr_{0.1}Ce_{0.7}Y_{0.1}Yb_{0.1}O_{3-\delta}$ (BZCYYb) membranes for hydrogen separation, Int. J. Hydrog. Energy 38 (2013) 14743–14749.
[6] S. Fang, K. Brinkman, F. Chen, Unprecedented CO_2-promoted hydrogen permeation in Ni–$BaZr_{0.1}Ce_{0.7}Y_{0.1}Yb_{0.1}O_{3-\delta}$ membrane, ACS Appl. Mater. Interfaces 6 (2014) 725–730.

[7] L. Barelli, G. Bidini, F. Gallorini, S. Servili, Hydrogen production through sorption-enhanced steam methane reforming and membrane technology: a review, Energy 33 (2008) 554–570.
[8] S.V. Bhide, A.V. Virkar, Stability of $BaCeO_3$-based proton conductors in water-containing atmospheres, J. Electrochem. Soc. 146 (1999) 2038–2044.
[9] N. Zakowsky, S. Williamson, J.T.S. Irvine, Elaboration of CO_2 tolerance limits of $BaCe_{0.9}Y_{0.1}O_{3-\delta}$ electrolytes for fuel cells and other applications, Solid State Ionics 176 (2005) 3019–3026.
[10] F. Chen, O.T. Sorensen, G. Meng, D. Peng, Chemical stability study of $BaCe_{0.9}Nd_{0.1}O_{3-\delta}$ high-temperature proton-conducting ceramic, J. Mater. Chem. 7 (1997) 481–485.
[11] L. Bi, Z. Tao, C. Liu, W. Sun, H. Wang, W. Liu, Fabrication and characterization of easily sintered and stable anode-supported proton-conducting membranes, J. Membr. Sci. 336 (2009) 1–6.
[12] F. Zhao, F. Chen, Performance of solid oxide fuel cells based on proton-conducting $BaCe_{0.7}In_{0.3-x}Y_xO_{3-\delta}$ electrolyte, Int. J. Hydrog. Energy 35 (2010) 11194–11199.
[13] A. Radojković, M. Žunić, S.M. Savić, G. Branković, Z. Branković, Enhanced stability in CO_2 of Ta doped $BaCe_{0.9}Y_{0.1}O_{3-\delta}$ electrolyte for intermediate temperature SOFCs, Ceram. Int. 39 (2013) 2631–2637.
[14] K. Xie, R. Yan, X. Liu, A novel anode supported $BaCe_{0.4}Zr_{0.3}Sn_{0.1}Y_{0.2}O_{3-\delta}$ electrolyte membrane for proton conducting solid oxide fuel cells, Electrochem. Commun. 11 (2009) 1618–1622.
[15] K. Xie, R.Q. Yan, X.Q. Liu, Stable $BaCe_{0.7}Ti_{0.1}Y_{0.2}O_{3-\delta}$ proton conductor for solid oxide fuel cells, J. Alloys Compd. 479 (2009) L40–L42.
[16] K. Xie, R. Yan, X. Xu, X. Liu, G. Meng, The chemical stability and conductivity of $BaCe_{0.9-x}Y_xNb_{0.1}O_{3-\delta}$ proton-conductive electrolyte for SOFC, Mater. Res. Bull. 44 (2009) 1474–1480.
[17] L. Bi, S. Zhang, S. Fang, Z. Tao, R. Peng, W. Liu, A novel anode supported $BaCe_{0.7}Ta_{0.1}Y_{0.2}O_{3-\delta}$ electrolyte membrane for proton-conducting solid oxide fuel cell, Electrochem. Commun. 10 (2008) 1598–1601.
[18] K.H. Ryu, S.M. Haile, Chemical stability and proton conductivity of doped $BaCeO_3$–$BaZrO_3$ solid solutions, Solid State Ionics 125 (1999) 355–367.
[19] L. Yang, S. Wang, K. Blinn, M. Liu, Z. Liu, Z. Cheng, M. Liu, Enhanced sulfur and coking tolerance of a mixed ion conductor for SOFCs: $BaZr_{0.1}Ce_{0.7}Y_{0.2-x}Yb_xO_{3-\delta}$, Science 326 (2009) 126–129.
[20] C. Zuo, S. Zha, M. Liu, M. Hatano, M. Uchiyama, $Ba(Zr_{0.1}Ce_{0.7}Y_{0.2})O_{3-\delta}$ as an electrolyte for low-temperature solid-oxide fuel cells, Adv. Mater. 18 (2006) 3318–3320.
[21] J. Yi, S. Feng, Y. Zuo, W. Liu, C. Chen, Oxygen permeability and stability of $Sr_{0.95}Co_{0.8}Fe_{0.2}O_{3-\delta}$ in a CO_2- and H_2O-containing atmosphere, Chem. Mater. 17 (2005) 5856–5861.
[22] I. Kaus, K. Wiik, B. Krogh, M. Dahle, K.H. Hofstad, S. Aasland, Stability of $SrFeO_3$-based materials in H_2O/CO_2-containing atmospheres at high temperatures and pressures, J. Am. Ceram. Soc. 90 (2007) 2226–2230.
[23] K. Efimov, O. Czuprat, A. Feldhoff, In-situ X-ray diffraction study of carbonate formation and decomposition in perovskite-type BCFZ, J. Solid State Chem. 184 (2011) 1085–1089.
[24] J. Yi, T.E. Weirich, M. Schroeder, CO_2 corrosion and recovery of perovskite-type $BaCo_{1-x-y}Fe_xNb_yO_{3-\delta}$ membranes, J. Membr. Sci. 437 (2013) 49–56.
[25] C.S. Tu, R.R. Chien, V.H. Schmidt, S.C. Lee, C.C. Huang, C.L. Tsai, Thermal stability of $Ba(Zr_{0.8-x}Ce_xY_{0.2})O_{2.9}$ ceramics in carbon dioxide, J. Appl. Phys. (2009), 103504-1–103504-7.
[26] W. Kaabar, S. Bott, R. Devonshire, Raman spectroscopic study of mixed carbonate materials, Spectrochim. Acta A 78 (2011) 136–141.
[27] X. Wang, G. Lu, Y. Guo, Y. Xue, L. Jiang, Y. Guo, Z. Zhang, Structure, thermal-stability and reducibility of Si-doped Ce–Zr–O solid solution, Catal. Today 126 (2007) 412–419.
[28] K.S. Blinn, H. Abernathy, X. Li, M. Liu, L.A. Bottomley, M. Liu, Raman spectroscopic monitoring of carbon deposition on hydrocarbon-fed solid oxide fuel cell anodes, Energy Environ. Sci. 5 (2012) 7913–7917.
[29] C.M. Chun, J.D. Mumford, T.A. Ramanarayanan, Carbon-induced corrosion of nickel anode, J. Electrochem. Soc. 147 (2000) 3680–3686.
[30] V. Alzate-Restrepo, J.M. Hill, Carbon deposition on Ni/YSZ anodes exposed to CO/H_2 feeds, J. Power Sources 195 (2010) 1344–1351.
[31] C. Binet, M. Daturi, J.C. Lavalley, IR study of polycrystalline ceria properties in oxidised and reduced states, Catal. Today 50 (1999) 207–225.
[32] C.W. Tanner, A.V. Virkar, Instability of $BaCeO_3$ in H_2O-containing atmospheres, J. Electrochem. Soc. 143 (1996) 1386–1389.
[33] Y. Li, Q. Fu, M. Flytzani-Stephanopoulos, Low-temperature water-gas shift reaction over Cu- and Ni-loaded cerium oxide catalysts, Appl. Catal. B 27 (2000) 179–191.
[34] C. Wheeler, A. Jhalani, E.J. Klein, S. Tummala, L.D. Schmidt, The water-gas shift reaction a